

ARTICLE

Open Access

Flexible pressure sensors with ultrahigh stress tolerance enabled by periodic microslits

Song Wang¹, Chenying Wang^{2✉}, Yifan Zhao^{2✉}, Yujing Zhang¹, Yaxin Zhang¹, Xiangyue Xu¹, Qijing Lin², Kai Yao³, Yuheng Wang³, Feng Han², Yu Sun⁴ and Zhuangde Jiang¹

Abstract

Stress tolerance plays a vital role in ensuring the effectiveness of piezoresistive sensing films used in flexible pressure sensors. However, existing methods for enhancing stress tolerance employ dome-shaped, wrinkle-shaped, and pyramidal-shaped microstructures in intricate molding and demolding processes, which introduce significant fabrication challenges and limit the sensing performance. To address these shortcomings, this paper presents periodic microslits in a sensing film made of multiwalled carbon nanotubes and polydimethylsiloxane to realize ultrahigh stress tolerance with a theoretical maximum of 2.477 MPa and a sensitivity of 18.092 kPa⁻¹. The periodic microslits permit extensive deformation under high pressure (e.g., 400 kPa) to widen the detection range. Moreover, the periodic microslits also enhance the sensitivity based on simultaneously exhibiting multiple synapses within the sensing interface and between the periodic sensing cells. The proposed solution is verified by experiments using sensors based on the microslit strategy for wind direction detection, robot movement sensing, and human health monitoring. In these experiments, vehicle load detection is achieved for ultrahigh pressure sensing under an ultrahigh pressure of over 400 kPa and a ratio of the contact area to the total area of 32.74%. The results indicate that the proposed microslit strategy can achieve ultrahigh stress tolerance while simplifying the fabrication complexity of preparing microstructure sensing films.

Introduction

Significant progress has been made recently in the development of flexible pressure sensors that mimic the pressure-sensing capabilities of human skin and collect environmental data^{1–3}. These advanced sensors have been widely applied in various fields, including human-computer interaction^{4–9}, health monitoring^{10–13}, and intelligent robotics^{14,15}. Flexible piezoresistive pressure sensors have been widely used because of their simple manufacturing process, capability to record signals, and

affordability. One of the common ways to achieve sensing films with excellent mechanical properties, stability, and durability is to incorporate conductive nanoparticles into an elastic matrix as a sensing material^{16,17}. Typically, carbon-based nanomaterials, such as carbon black^{18,19}, carbon fibers⁸, and graphene^{20,21}, are conventionally used as conductive fillers. Additionally, carbon nanotubes (CNTs) offer excellent electrical properties, low density, and high elasticity, making them advantageous for sensors in terms of sensitivity, robustness, and stability compared to other materials^{17,22–25}. Particularly, multiwalled carbon nanotubes (MW-CNT) have been considered highly promising due to their exceptional electromechanical performance and ease of preparation compared to single-walled carbon nanotubes²⁶.

Recently, various strategies have been proposed for improving the stress tolerance of piezoresistive flexible pressure sensors and expanding their sensitivity, including pyramidal^{27,28}, dome-shaped²⁹, wrinkled³⁰, and

Correspondence: Chenying Wang (wangchenying@mail.xjtu.edu.cn) or Yifan Zhao (zhaoyifan100@mail.xjtu.edu.cn)

¹State Key Laboratory for Manufacturing Systems Engineering, International Joint Laboratory for Micro/Nano Manufacturing and Measurement Technologies, School of Mechanical Engineering, Xi'an Jiaotong University, Xi'an, China

²State Key Laboratory for Manufacturing Systems Engineering, International Joint Laboratory for Micro/Nano Manufacturing and Measurement Technologies, School of Instrument Science and Technology, Xi'an Jiaotong University, Xi'an, China

Full list of author information is available at the end of the article

© The Author(s) 2024



Open Access This article is licensed under a Creative Commons Attribution 4.0 International License, which permits use, sharing, adaptation, distribution and reproduction in any medium or format, as long as you give appropriate credit to the original author(s) and the source, provide a link to the Creative Commons license, and indicate if changes were made. The images or other third party material in this article are included in the article's Creative Commons license, unless indicated otherwise in a credit line to the material. If material is not included in the article's Creative Commons license and your intended use is not permitted by statutory regulation or exceeds the permitted use, you will need to obtain permission directly from the copyright holder. To view a copy of this license, visit <http://creativecommons.org/licenses/by/4.0/>.

Table 1 Summary of different microstructures and their fabrication methods and pressure sensing performance

Ref.	Microstructure type	Preparation methods	Sensing range		
			Experimentally/ Maximum (kPa)	Theoretical maximum (MPa)	
44	Fingerprint-microstructure	Laser manufacturing & Magnetron sputtering & Dipping	0–4.5	4.5	–
45	Strip-shaped bulges	Demolding from leaves & Chemical vapor deposition & Film transfer and conformal covering	0–5.8	5.8	–
41	Multistage ridges	Demolding from leaves & Thermally evaporating	0–7	7	–
33	Tentacle-like conical micropillars	Laser-engraving & Scratch coating & Demolding	0–23	23	–
32	Micro Cone Array	Two-step demolding process from leaves & Spray-coating	0.2–25	25	–
46	Bionic hierarchical structure	Demolding from abrasive papers & Depositing	0–90	90	–
4	Microdome	Two-step demolding process from rose petal & Sputtering	0.058–98.7	98.7	–
35	Pollen-shaped	Two-step demolding process from pollen & Drop-casting	0–218	218	–
47	Hemispherical arrays and gradient pores	Four-step pressing & Demolding & Removing the sacrificial template	0–400	400	–
This work	Microslits	Screen printing	0–400	400	2.477

hierarchical configurations^{31–34}. These innovative designs have shown promising application potential, but their fabrication process often involves complex molding and demolding processes with cumbersome coating and molecular self-assembly steps (SAMs)³⁵.

For practical applications, pressure sensors should be flexible and sensitive and have a wide detection range. A common strategy for improving the stress tolerance of pressure sensors has been to fabricate continuous microstructures interfacially^{36–39}. However, when an externally applied pressure is exerted, the force is concentrated at the root of the continuous microstructures^{28,40,41}, which can lead to distortions within adjacent cells and limit the sensing range. An overview of the existing flexible pressure sensors with diverse microstructures and their fabrication techniques is presented in Table 1. Nevertheless, in the preparation of these sensors, complex molding and demolding processes are performed, and continuous microstructures limit the sensing performance. In this study, a reasonable prediction of a 2.477 MPa pressure tolerance is achieved for the contact area using the in situ observation method.

It is hypothesized that introducing sufficient space to permit extra deformation between continuous microstructural cells can help to enhance stress tolerance in a sensing film. To test this hypothesis, microslits are constructed in the sensing film during the screen printing process to achieve ultrahigh stress tolerance. A sensing film, MW-CNT/polydimethylsiloxane (PDMS), with a periodic microslit morphology was developed with an

ultrahigh stress tolerance of 400 kPa experimentally and a theoretical maximum stress tolerance of 2.477 MPa, and a sensitivity of 18.092 kPa⁻¹ is achieved. The microslits in the MW-CNT/PDMS sensing film permit extensive deformation without requiring molding and demolding processes, leading to a distortion of only 26.7% (contact area/total area, CA/TA) under a high pressure of 400 kPa. Moreover, optimal ratios of MW-CNT/PDMS ensure multiple contacts successively in the sensing film and between the periodic sensing cells under loading, which enhances the sensing performance. The developed devices are employed for monitoring wind directions under a minute pressure. They also show reliable performance in medium-pressure sensing applications, such as robot movement and human health monitoring. Importantly, a vehicle load check is achieved for ultrahigh pressure sensing under an ultrahigh pressure of over 400 kPa and a maximal CA/TA ratio of 32.74%. The facile fabrication process of screen printing coupled with the proposed innovative microslit design has significant application potential in guiding the development of flexible devices that can withstand high-level stress.

Results and discussion

The structure of the proposed sensor is presented in Fig. 1a. The sensor comprises flexible electrodes, support and bonding layers, a sensing film, and a protective layer. The sensing films were prepared employing screen printing technology using a mixture of MW-CNT and PDMS (refer to Fig. S1). The approach allows for

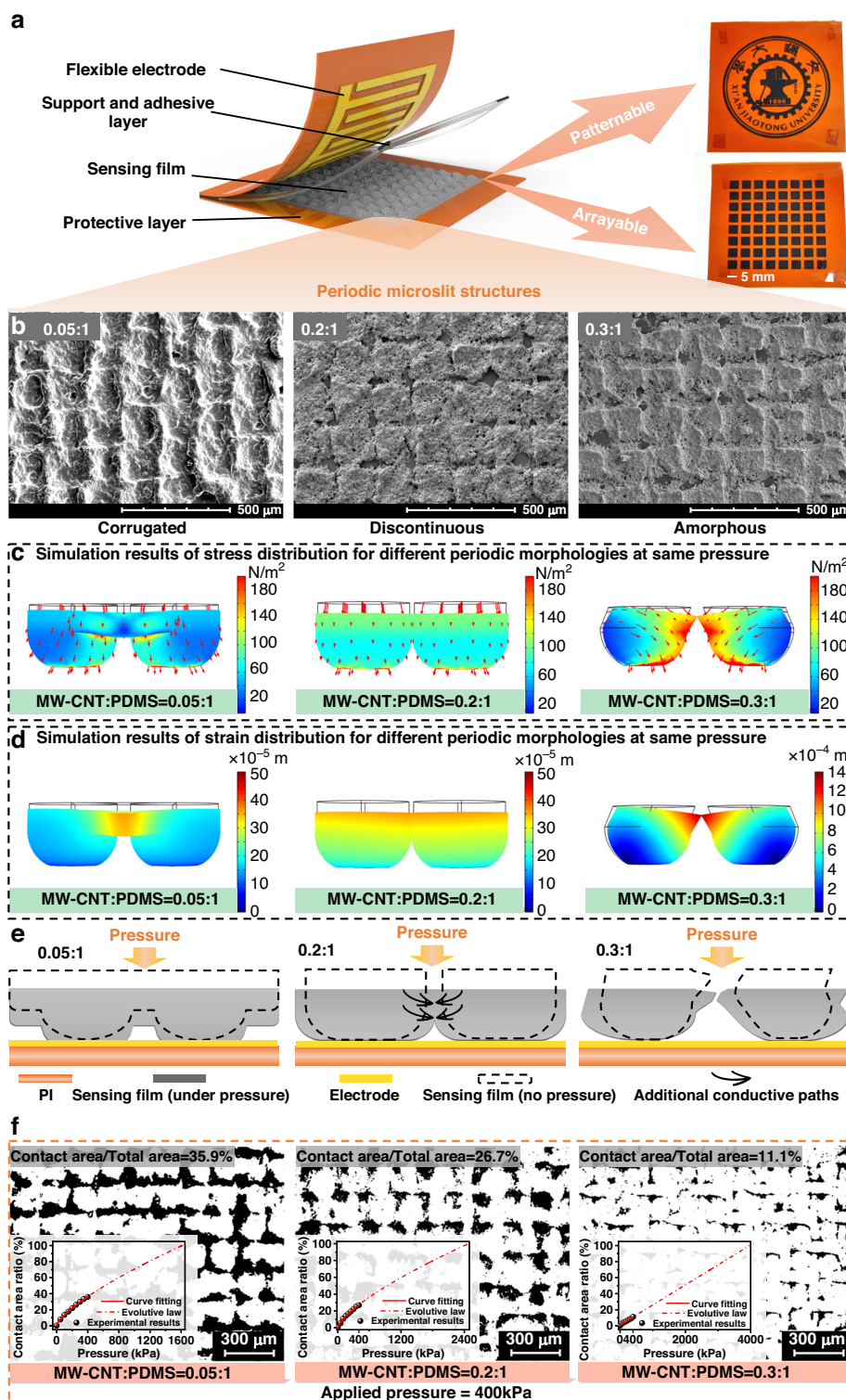


Fig. 1 The sensor structure and characterization of the sensing film. **a** Structural diagram of the sensor facilitating patterning and array construction; **b** SEM images of the NW-CNT/PDMS sensing film with different weight ratios; the scale of all SEM images is 500 μm ; **c** the simulated models of stress; **d** the simulated models of strain distributions; **e** schematic evolution in a distinct NW-CNT/PDMS sensing film; **f** the ratio of the contact area to the total area in the in situ measurement under an applied pressure of 400 kPa; the dark region represents the contact area, and the insets show the variations in the ratio with the applied pressure changing from zero to 400 kPa

straightforward patterning and arraying of sensing films, as illustrated in the right insets in Fig. 1a. Similarly, the Raman spectra of a well-blended film of PDMS and MW-CNT are presented in Fig. S2. Figure S3 shows that the film is lightweight and bendable and can be attached to bent fingers and leaf surfaces. The scanning electron microscopy (SEM) images in Fig. 1b and S4 indicate the presence of microslits in the MW-CNT/PDMS sensing films and show that microslits have been manifested successfully. In this study, various distinctive periodic microslit morphologies were observed by introducing microslits into sensing films with different MW-CNT/PDMS weight ratios. These morphologies were observed under the combined influence of the flowability of the complexes and the mold action of the screen-printed plates. In particular, the widths of the microslits of the sensing films increased with the MW-CNT/PDMS ratio. In addition, the introduction of the optimal microslits morphology led to a discontinuous square shape of the sensing morphology, with a ratio of 0.2:1. In contrast, as the ratio decreased, the morphology of the sensing film exhibited a continuous corrugation (a ratio of 0.05:1) without microslits; in contrast, when the ratio increased, it exhibited an unformed morphology (a ratio of 0.3:1) with widest microslits. Based on the results, the synergistic effect of the microslits and MW-CNT/PDMS is concluded to dominate the transition of the sensing morphology. To understand the mechanisms underlying the superior stress tolerance and sensitivity achieved in the film with a well-designed periodic microslits structure, twofold analysis was conducted. First, it is considered that the microslits configuration enables an extensive deformation to widen the detection range; second, it is considered that microslits synergize with the hierarchical microstructure to amplify the contact area during compression, which results in enhanced sensitivity.

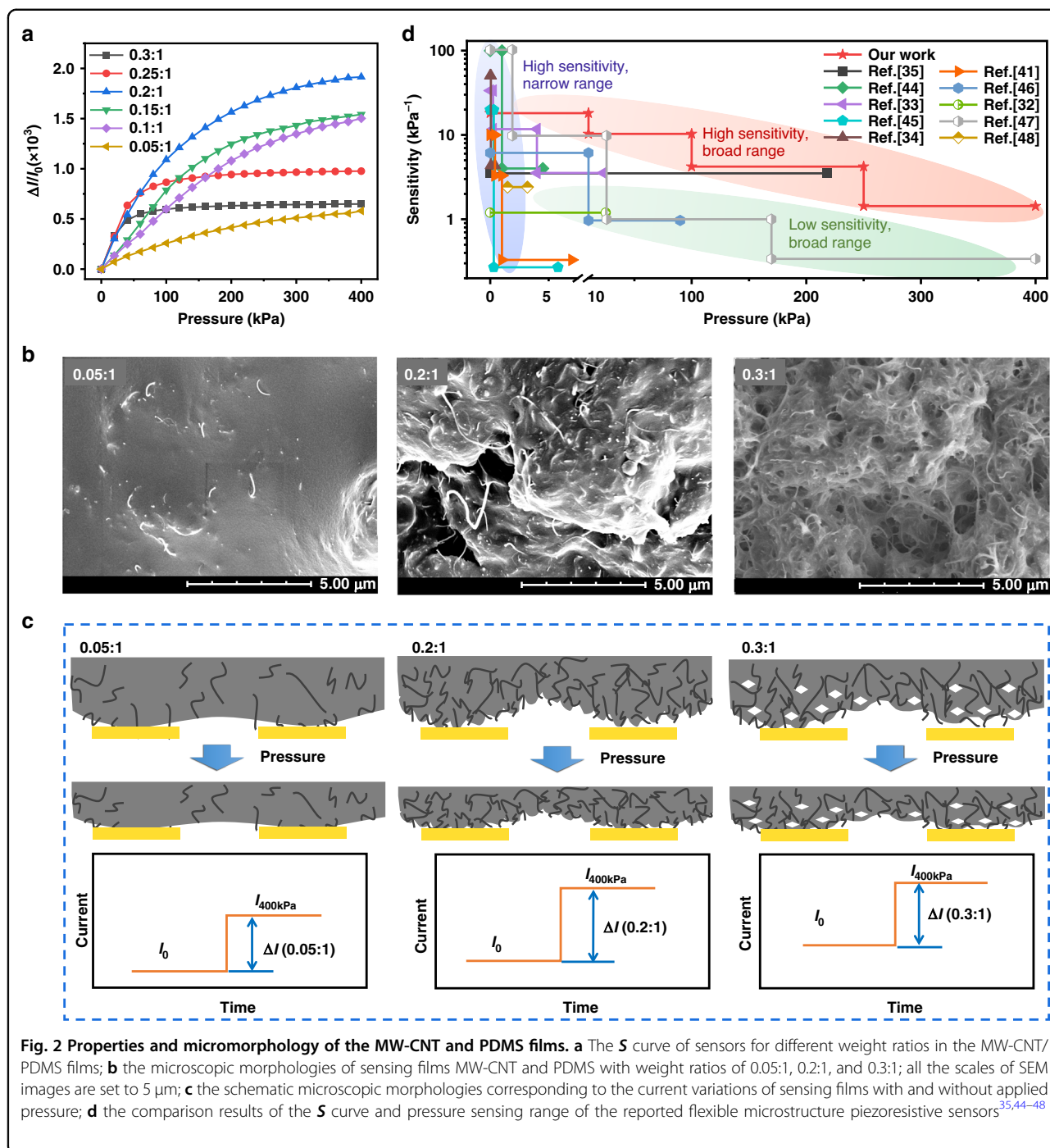
The proposed sensing mechanism was proven as follows. First, finite element modeling (described in the Supporting Information) was used to simulate mechanical models for stress and strain distributions for different types of periodic microstructure morphologies observed in the SEM images, as shown in Fig. 1c, d. When pressure was applied, the adjacent corrugations in the MW-CNT/PDMS (0.05:1) sensing film without microslits were squeezed compactly, thus resulting in nonhomogeneous distributions of mechanical properties. The phenomenon that the stress and strain distortion could occur at the root contact area demonstrated that the forces and deformations were not adequately released because of limited available space between the adjacent periodic structures under pressure. The same tendency of nonhomogeneous distributions was observed in the MW-CNT/PDMS (0.3:1) sensing film with the largest microslits, but it exhibited larger variations in forces and deformations compared to the MW-CNT/

PDMS (0.05:1) sensing film. This occurred because that amorphous morphologies originated from the collapse of the quadrate structure, causing an unbalanced distribution of stress and strain. However, symmetrical and balanced distributions of stress and strain occurred in the well-designed sensing film with MW-CNT/PDMS (0.2:1). This could be attributed to the presence of well-designed microslits that helped maintain the stability of periodic square structures. These suitable microslits could not only enable the homogeneous distribution of stress and strain throughout the film but also generate additional conductive paths (multiple synapses) when subjected to pressure, as shown in the evolution process illustrated in Fig. 1e. This further proved that the well-designed microslits could ensure superior sensing performance while enhancing stress tolerance. Furthermore, the in situ setup method (Fig. S5) with a maximal pressure of 400 kPa was employed for monitoring the stress tolerance of the sensing film under pressure to validate the simulation results. The endurance of applied pressure in the sensing film was quantified using the ratio of the contact area (CA under pressure) to the total area (TA tested area) of the sensing film, as shown in Fig. 1f. Ratios of 35.9% and 26.7% were detected in the MW-CNT/PDMS (0.05:1) and MW-CNT/PDMS (0.2:1) sensing films under a pressure of 400 kPa, respectively. This indicated that the MW-CNT/PDMS (0.2:1) sensing film with well-designed microslits had smaller deformation compared to the MW-CNT/PDMS (0.05:1) sensing film, reflecting its greater ability to endure higher pressure (maximum 2.477 MPa). Generally, the MW-CNT/PDMS (0.3:1) film exhibited wider microslits due to its unstable and irregular morphology. This characteristic allowed greater accommodation of microstructure deformation, resulting in enhanced resistance to the applied pressure. Consequently, the MW-CNT/PDMS (0.3:1) sensing film showed the lowest ratio of 11.1% under an applied pressure of 400 kPa. However, it should be noted that wider gaps between periodic cells of the MW-CNT/PDMS (0.3:1) sensing film impeded signal sensing, as shown in Fig. 2a. Therefore, the results provided strong experimental evidence that the MW-CNT/PDMS (0.2:1) sensing film could endure stress force and strain deformation, ensuring optimal sensing performance.

Next, the sensitive performance of the MW-CNT/PDMS sensing film was evaluated. The sensitivity performance of different sensor devices with different periodic morphologies is presented in Fig. 2a. The sensitivity (S) of the sensor device was calculated as:

$$S = \frac{\Delta I / I_0}{\Delta P} \quad (1)$$

where ΔI represents the difference between the current value under the applied pressure (I) and the initial value



without applied pressure (I_0), and it is calculated as $\Delta I = I_0 - I$; ΔP is the pressure applied to the sensor.

Thus, the shift in the current is significant for S . The current-voltage ($I-V$) curves of the sensor presented in Fig. S6 show linear variations, indicating an ohmic contact between the sensing film and the electrodes. This linear behavior indicated that the micromorphologies of the contact resistance had a significant effect on the sensing performance. To further demonstrate the impact of the

well-designed microslits on sensitivity, Figure S7 presents the sensing mechanism of the microslits pressure sensor. The initial resistance of the sensor when uncompressed was calculated as:

$$R = R_a + R_b + R_c + R_d \tag{2}$$

where R_a , R_b , R_c , and R_d represent the resistance of electrodes, the contact resistance between the sensing film

and electrodes, the bulk resistance of a sensing film, and the contact resistance between the periodic sensing cells, respectively.

When the sensor was subjected to external pressure, the microstructure of the sensing film was compressed and deformed, increasing the contact area between the sensing film and the electrodes and that between the periodic sensing cells, as shown in Fig. 1c, d; the evolution process is illustrated in Fig. 1e. Furthermore, the values of R_b and R_d decrease with the contact area, so these values denote critical factors affecting the sensor sensitivity. However, the variations in the R_a and R_c values were considerably smaller than those of R_b and R_d , which indicated that these terms could be neglected. Therefore, the sensitivity of the sensor was obtained as:

$$S = \frac{I-I_0}{I_0} = \frac{I}{I_0} - 1 = \frac{U/R}{U/R_0} - 1 = \frac{R_0}{R} - 1 = \frac{R_{b0}+R_{d0}}{R_b+R_d} - 1 \quad (3)$$

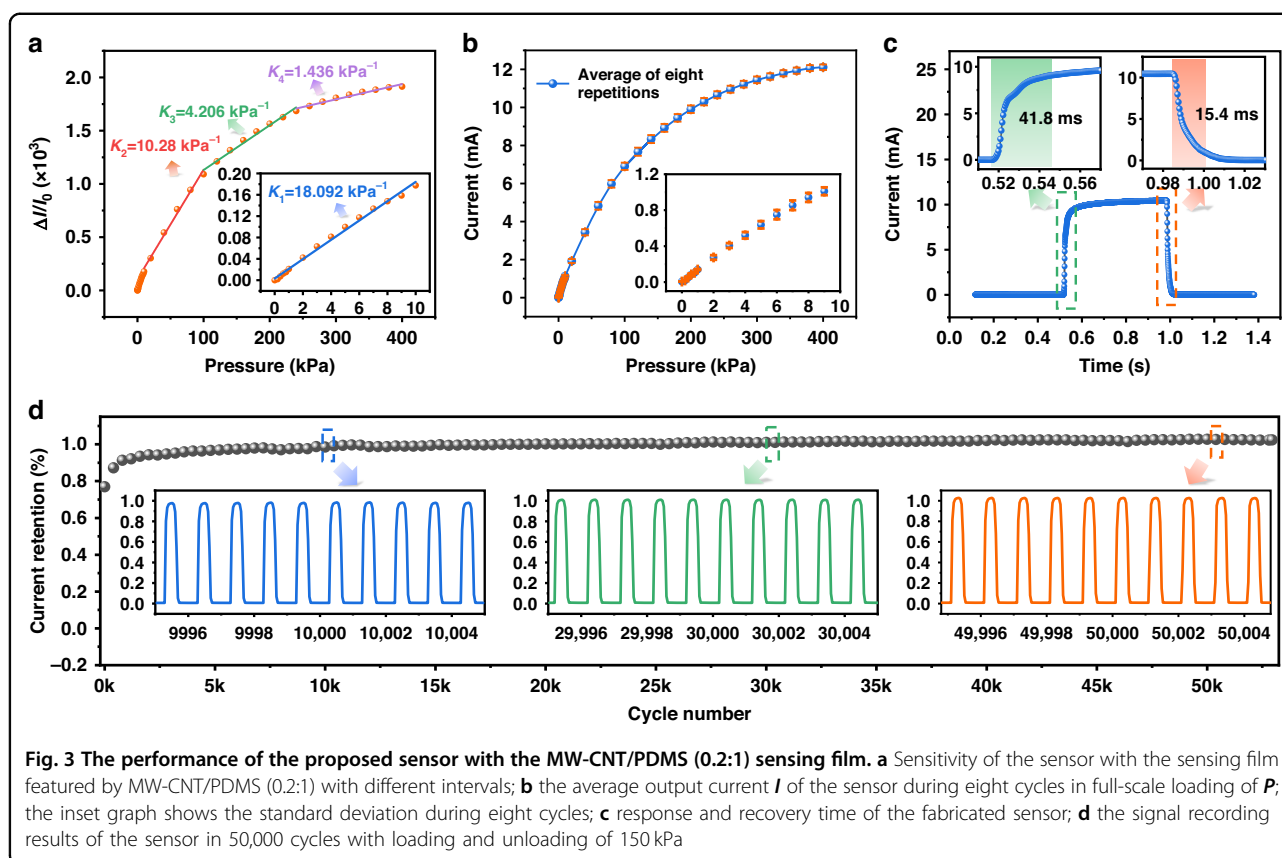
where U represents the bias voltage; R and R_0 denote the resistance of a sensing film under applied pressure and its initial value without any pressure applied; and R_{b0} and R_{d0} represent the initial values of resistances R_b and R_d , respectively.

From this equation, the sensitivity was positively correlated with the variations in the contact area between the sensing film and electrodes and that between the periodic sensing cells.

As shown in Fig. 2a, the MW-CNT/PDMS sensing film (0.2:1) exhibited the best sensitivity over the entire range (0–400 kPa) among all of the films. This enhanced sensitivity is attributed to the well-designed microslits that caused variations in the R_d value and the hierarchical microstructure morphology in each periodic structural cell, leading to changes in the R_b value, as shown in the SEM images in Fig. 2b. As presented in Fig. 2b, when the MW-CNT were doped into the PDMS in infinitesimal amounts, a smooth surface of the MW-CNT/PDMS films (0.05:1) with several carbon nanotubes was observed. However, the discrepancies became even more noticeable as the doping amounts of MW-CNT increased. The intricate hierarchical morphologies could be obtained in both MW-CNT/PDMS films (0.2:1 and 0.3:1) so that the new contacts in the interface of the sensing film could be reproduced abundantly under the applied pressure. This resulted in the lowest S value in the MW-CNT/PDMS films (0.05:1) because the nearly smooth surface and the continuous structure without microslits, shown in Fig. 1b, could not afford extra contacts under the applied pressure. The MW-CNT/PDMS films (0.3:1) were expected to obtain the highest S values of all the tested films because of their complex and compact substructures; however, an unexpected consequence of S arose to hinder the

performance of these films. As illustrated in Fig. 2b, multiple holes were observed in the SEM image of the MW-CNT/PDMS films (0.3:1), and these holes in the sensing film increased the sensor resistance under P . The exceptionally wide microslits posed a challenge in establishing a cell-to-cell contact. These factors both limited the output piezoresistive signals. Moreover, the massive introduction of the MW-CNT resulted in the highest I_0 in the MW-CNT/PDMS films (0.3:1), as displayed in Fig. 2c, which also limited sensitivity. In contrast, the SEM images of the MW-CNT/PDMS sensing film (0.2:1) showed that multiple holes were almost evaded and prevented. Finally, the highest ΔI in the MW-CNT/PDMS (0.2:1) confirmed that these films demonstrated the best sensing performance, which aligns with the trends of the curves as functions of S shown in Fig. 2a. The results in Fig. 2d demonstrate that the proposed sensor design was superior regarding the sensitivity and detection range to the other recently reported design. The outstanding performance of the proposed sensor design can be attributed to the introduction of suitable microslits and hierarchical sub-morphologies. These design features can effectively mitigate the excess forces and deformations while constructing the extra conducting paths.

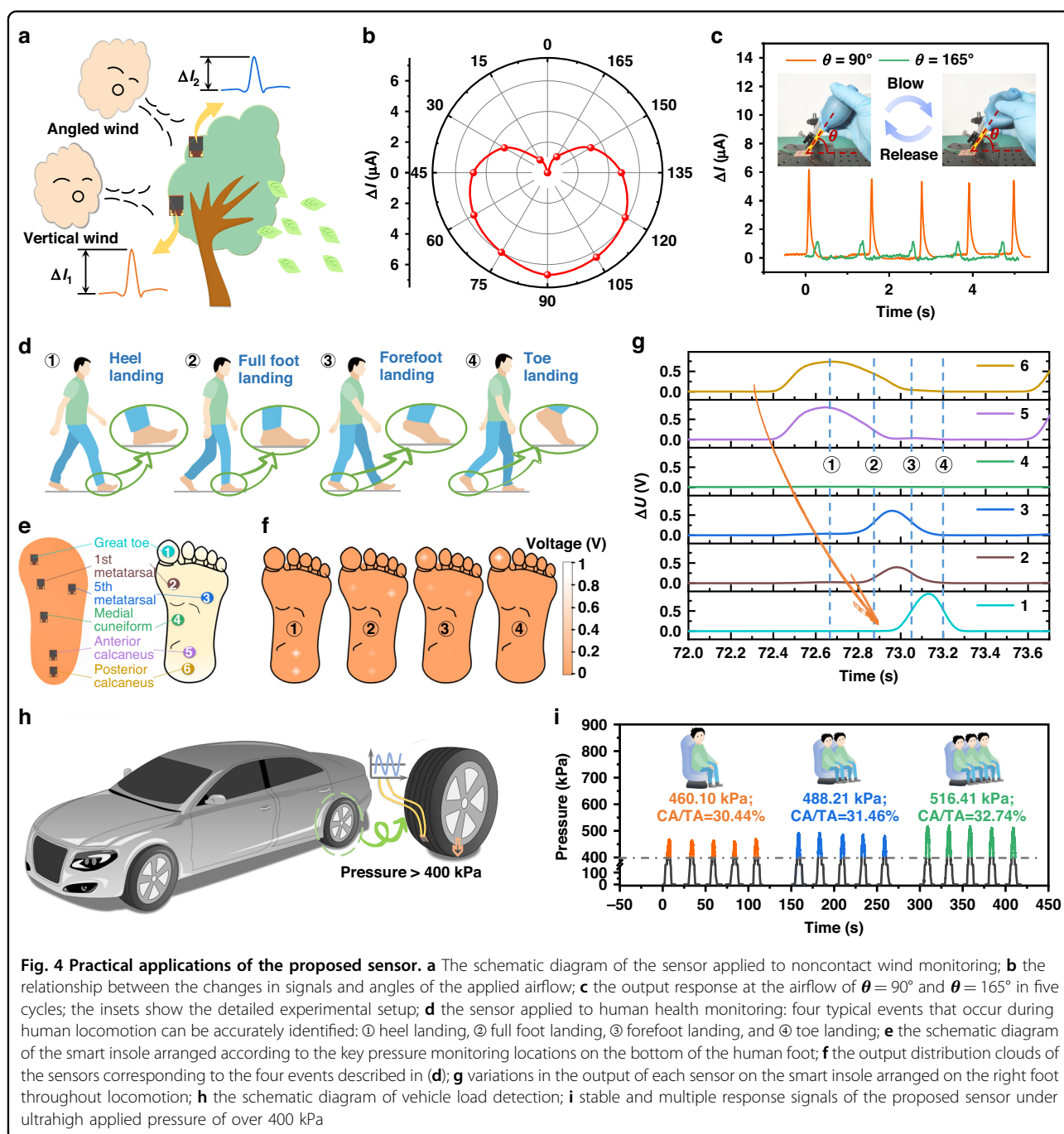
To explore potential applications of the sensor with periodic features in a sensing film, the S value was investigated within the pressure range of 0–400 kPa, as shown in Fig. 3a. The maximal S value of the sensor with the well-designed MW-CNT/PDMS (0.2:1) sensing film in different pressure intervals could be fitted to approximately 18.092 kPa^{-1} in the pressure range 0–10 kPa. As shown in Fig. 3a, the sensitivity slightly dropped to 10.28 kPa^{-1} ; additionally, a constant S value of 4.206 kPa^{-1} was exhibited when the applied pressure varied from 100 kPa to 250 kPa. Eventually, the sensitivity changed to 1.436 kPa^{-1} in the pressure range of 250 kPa–400 kPa. These results validated that the proposed sensor design is suitable for a variety of practical situations with different P values. Furthermore, the variations in the I value in the eight cycles with P from zero to 400 kPa are presented in Fig. 3b. The error bars in the inset graph in Fig. 3b represent the standard deviation of the measurement, which shows that the results of the eight cycles were uniform enough to achieve excellent robustness in sensing, which could be attributed to the superior stress tolerance of the squared periodic microslits in the MW-CNT/PDMS (0.2:1) film. Similarly, Fig. 3c presents the response and recovery time of the proposed sensor for the loading and unloading cases under an applied pressure of 150 kPa. The square step-shape response in the graph indicates an extremely fast response time of 41.8 ms and a recovery time of 15.4 ms. Figure 3d illustrates the remarkable stability of the sensor's current I across more than 50,000 loading and unloading cycles under an



applied pressure of 150 kPa, highlighting excellent stress tolerance and stability. The proposed microslit flexible pressure sensor exhibits hysteresis in its electrical response, as depicted in Fig. S8. This hysteresis is attributed to the viscoelastic nature of the MW-CNT and PDMS complex^{42,43}. The mixture film cannot immediately return to its original state after pressure is released, resulting in relatively low current retention in the initial state, as shown in Fig. 3d. Moreover, the responses of the sensor under different frequencies of 0.5 Hz, 1 Hz, 2 Hz, and 4 Hz at a pressure of 250 kPa are displayed in Fig. S9, where favorable consistency can be observed, which further reinforced the reliability and suitability of the proposed sensor for particular applications. Furthermore, as shown in Fig. S10, an 8×8 sensor array with a resolution of 6.5 mm was tested to identify the magnitude and distribution of the pressure when the letters Y, E, and S were applied. These results demonstrated the good application potential of the well-designed sensor in sensing monitoring over a large area. Furthermore, the results in Fig. S11 indicate the current response of the sensor over the temperature range from zero to 40°C. The proposed sensor exhibited a small sensing variation and was applicable in most of the daily scenarios with respect to the varied temperatures. Then, the output currents of

three samples of different batches were tested to verify the homogeneity. The calculated mean and standard deviation are shown in Fig. S12, which demonstrate good uniformity of the performance.

Figure 4a shows a noncontact sensing application based on the sensing performances achieved using the proposed periodic microslits design in the MW-CNT/PDMS film. In this application, a sensor was fixed on the leaves that could be distorted arbitrarily in a windy atmosphere. This design represents a feasible approach to quantitatively analyze the ambient wind direction due to the introduction of the microslit design in the sensing film, leading to excellent deformation capacity. Hence, the ambient airflow was experimentally imitated, and a schematic of the wind direction detection process is shown in Fig. 4c. The airflow angles (θ) applied to the sensor could be switched from zero to 180° to follow the realistic atmosphere. Furthermore, as presented in Fig. 4b, when the airflow angles were horizontally shifted from zero and 180° to the vertical (90°) direction, the output of the sensor showed an increasing trend, achieving the maximum signal recording in the vertical direction. The heart-shaped sensing loop depicts the distinct variation to differentiate the directions of airflows. Figure 4c also demonstrates the stability and repeatability of wind direction detection at θ values of 90°



and 165° , respectively. Additionally, Figure S13 shows that the sensor output current increases with the airflow strength, indicating its suitability for monitoring wind magnitude. Therefore, by combining multiple sensors, it is possible to simultaneously monitor both wind strength and direction. These results validate that the presence of periodic microslit structures in a sensing film can support noncontact sensor application by outputting recognizable tiny signals. Furthermore, the designed sensor also

demonstrates its capability in detecting robot finger joint bending, grasping objects, walking postures, and pulses for conventional contact applications, as shown in Figs. S14 and S15. Considering the deformation of the sensor in several application scenarios, it is crucial to explore the shift in sensing performance before and after repeated deformation. From Fig. S16, the favorable sensor performance can be maintained by bending over 1000 cycles. This indicates that our strategy of microslits makes the sensor exhibit an

outstanding ability to resist deformation. Furthermore, Fig. 4d shows the application of the proposed sensor in analyzing the foot-landing action in a gait cycle. This action can be divided into four stages: heel landing, full foot landing, forefoot landing, and toe landing. In this experiment, the sensors were installed on the PI substrate to make a smart insole, as shown in Fig. 4e. The detailed pressure distributions and the output signal of the proposed sensors are presented in Fig. 4f, which shows that the proposed sensor could accurately distinguish the motion states of the four stages in Fig. 4d. Figure S17 presents the stabilized output signals of each sensor during 96 normal walking gait cycles. One of the gait cycle signals (from 72.0 s to 73.7 s) was selected and analyzed, as plotted in Fig. 4g, where the four blue dashed lines represent the four stances shown in Fig. 4d. The rapid response and recovery capabilities of the proposed sensors allowed for sequential pressure increases from sensor 6 to sensor 1 (except for sensor 4), which is highlighted by the orange arrow in Fig. 4g. This result was consistent with the motion evolution from the heel contact to the toes being lifted off the ground. By using the pressure measurements at the medial cuneiform, pronation and supination could be diagnosed at an early stage. As shown in Fig. 4g, the signal of sensor 4 changed slightly during the considered action, indicating a neutral gait and no abnormalities. This result further confirmed that the proposed periodic microslits in the sensing film could help to obtain distinct response signals accurately for different parts of the soles, thus realizing gait health monitoring. Importantly, vehicle load detection could also be achieved using the sensor devices with the designed microslits, as illustrated in Fig. 4h, i. The distinct average pressures of 466.10 kPa, 488.21 kPa, and 516.41 kPa were utilized to determine the weights of vehicles for varying numbers of passengers. The corresponding CA/TA ratios for these pressures are 30.44%, 31.46%, and 32.74%, respectively, and were calculated based on the middle inset of Fig. 1f. The results indicated that the proposed sensor could still maintain stable functionality even under pressures exceeding 400 kPa (i.e., CA/TA of 26.7%) in practical applications. According to the results, the microslits in a sensing film are beneficial to holding the structural deformation under ultrahigh pressure, achieving robust pressure tolerance. The abovementioned results demonstrate that the proposed microslits fabricated in the sensing film could be a viable strategy for realizing accurate, sensitive, and real-time monitoring of the ambient atmosphere, human health diagnosis of diseases, and loading detection.

Conclusion

This paper presents the successful preparation of a piezoresistive sensing film made of MW-CNT/PDMS with periodic microslits. Based on the synergistic effect of the microslits and submicrostructures in sensing

performance, the fabricated sensor exhibits remarkable properties, such as an ultrahigh stress tolerance achieved under a pressure of 400 kPa and a theoretical maximum of 2.477 MPa, as well as a good sensitivity of 18.092 kPa^{-1} in the pressure range of 0–10 kPa. Simulation results and in situ observations demonstrate that the proposed sensing film can effectively accommodate deformation and achieve stress relief under applied pressure to widen the detection range. In addition, the film displacement expands uniformly in all directions, and additional contacts are formed between adjacent cells, thereby enhancing the sensitivity. The outstanding stability of the proposed sensor is demonstrated and validated using experiments with more than 50,000 load/unload cycles. The effectiveness of the proposed sensor in practical applications is therefore experimentally validated in testing that evaluates the proposed sensor's performance for detecting weak wind signals, supporting health monitoring, and detecting vehicle load. Finally, the findings of this study offer valuable insights into the design and fabrication of flexible devices with ultrahigh stress tolerance and thus contribute to the realization of ubiquitous and diversified pressure monitoring in the future.

Experimental section

Materials and reagents

PDMS and its curing agent were purchased from Dow Corning (Sylgard 184), America. MW-CNT with a purity of 95%, a length of $10 \mu\text{m}$ – $30 \mu\text{m}$, and a diameter of 10 – 20 nm were purchased from Jiangsu XFNano Materials Tech. Co., Ltd., China. Terpineol was purchased from Wuxi Yatai United Chemical Co., Ltd., China. The PI film with different thicknesses was purchased from Shanghai Texiang Electrical Insulation Materials Co., Ltd., China.

Preparation of sensing films with periodic microslit structures

The sensing films used in this study were prepared using screen printing technology, as illustrated in Fig. S1. The fabrication process involved mechanically mixing the MW-CNT and PDMS to create a mixture. The weight ratio of the MW-CNT to the PDMS was varied to examine its influence on the proposed sensor's performance. Particularly, for the mixtures with MW-CNT, PDMS weight ratios of 0.05:1, 0.1:1, 0.15:1, 0.2:1, 0.25:1, and 0.3:1 were prepared. In the hybrid slurry, MW-CNT were selected as a conductive component because of the high aspect ratio and high conductivity, which made it easier to form conductive pathways in the polymer matrix. Then, terpineol was added to adjust the viscosity of the composite to make it suitable for screen printing. Subsequently, the sensing film layer patterns ($1 \text{ cm} \times 1 \text{ cm}$) were screen printed. The film was heated to $120 \text{ }^\circ\text{C}$ to evaporate the excess solvent. The different microslit structures were

shaped by the synergy of the mesh blocking and the flow leveling of the mixture with different weight ratios.

Characterization

The microstructure and surface topography of all the sensing films were analyzed using field emission SEM (SU-8010, Hitachi, Ltd., Japan). The changes in the colloidal chemical structure before and after the addition of carbon nanotubes were measured using Raman spectroscopy. Specifically, a LabRAM HR evolution instrument from Horiba Scientific, Japan, was employed for this analysis. Furthermore, the changes in the contact area in the sensing were observed using an inverted metallographic microscope (model IE500M) from Sunny Optical Technology (Group) Co., Ltd., China.

Mechanical and electrical measurements

To measure the currents of the sensors, a bias voltage of 0.1 V was applied, and the resulting current was measured using a source measure unit (2450, Keithley Instruments, USA). The sensitivity curve of the sensor was obtained using a compression loading machine (PT-990T, ChemInstruments International Instruments, China). This machine was used to apply pressure to the sensor and record the corresponding current changes. The specific test methods and schematics are displayed in Fig. S18. To facilitate signal acquisition, the circuit shown in Fig. S10b was employed. This circuit was designed to convert the resistance of the sensor to a voltage in the sensor array and application tests. To investigate and evaluate the response time and stability of the proposed sensor under cyclic loads, the experimental setup presented in Fig. S19 was utilized. The setup could apply dynamic pressure to the sensor, accurately simulating real-world conditions.

Acknowledgements

This work was supported by the National Key R&D Program of China (Grant No. 2022YFB3204800).

Author details

¹State Key Laboratory for Manufacturing Systems Engineering, International Joint Laboratory for Micro/Nano Manufacturing and Measurement Technologies, School of Mechanical Engineering, Xi'an Jiaotong University, Xi'an, China. ²State Key Laboratory for Manufacturing Systems Engineering, International Joint Laboratory for Micro/Nano Manufacturing and Measurement Technologies, School of Instrument Science and Technology, Xi'an Jiaotong University, Xi'an, China. ³The Faculty of Electrical Engineering and Computer Science, Ningbo University, Ningbo, China. ⁴Department of Mechanical and Industrial Engineering, University of Toronto, Toronto, Canada

Author contributions

S.W. proposed the sensor design and drafted the manuscript. C.W. and Yi.Z. assisted in conceiving the study and helped draft the manuscript. Yu.Z., Ya.Z., and X.X. participated in the design of the circuit and performed data analysis. K.Y. and Y.W. conducted the simulation. Q.L. and F.H. provided technical support in the fabrication and characterization. Y.S. and Z.J. managed the research activity planning and execution.

Competing interests

Zhuangde Jiang and Yu Sun are editorial board members of the journal, no other author has reported any competing interest.

Supplementary information The online version contains supplementary material available at <https://doi.org/10.1038/s41378-023-00639-4>.

Received: 21 July 2023 Revised: 24 October 2023 Accepted: 15 November 2023

Published online: 08 February 2024

References

- Bae, G. Y. et al. Linearly and highly pressure-sensitive electronic skin based on a bioinspired hierarchical structural array. *Adv. Mater.* **28**, 5300–5306 (2016).
- Chen, W. & Yan, X. Progress in achieving high-performance piezoresistive and capacitive flexible pressure sensors: a review. *J. Mater. Sci. Technol.* **43**, 175–188 (2020).
- Hua, Q. et al. Skin-inspired highly stretchable and conformable matrix networks for multifunctional sensing. *Nat. Commun.* **9**, 244 (2018).
- Yang, T. et al. Hierarchically microstructure-bioinspired flexible piezoresistive bioelectronics. *ACS Nano* **15**, 11555–11563 (2021).
- An, B. W., Heo, S., Ji, S., Bien, F. & Park, J. Transparent and flexible fingerprint sensor array with multiplexed detection of tactile pressure and skin temperature. *Nat. Commun.* **9**, 2458 (2018).
- Feng, B. et al. Nacre-inspired, liquid metal-based ultrasensitive electronic skin by spatially regulated cracking strategy. *Adv. Funct. Mater.* **31**, 2102359 (2021).
- Chen, S. et al. Pruney fingers-inspired highly stretchable and sensitive piezoresistive fibers with isotropic wrinkles and robust interfaces. *Chem. Eng. J.* **430**, 133005 (2022).
- Zhong, M. et al. Wide linear range and highly sensitive flexible pressure sensor based on multistage sensing process for health monitoring and human-machine interfaces. *Chem. Eng. J.* **412**, 128649 (2021).
- Kim, S. et al. Wearable, ultrawide-range, and bending-insensitive pressure sensor based on carbon nanotube network-coated porous elastomer sponges for human interface and healthcare devices. *ACS Appl. Mater. Inter.* **11**, 23639–23648 (2019).
- Wu, X. et al. Large-area fabrication of high-performance flexible and wearable pressure sensors. *Adv. Electron. Mater.* **6**, 1901310 (2020).
- Lu, P. et al. Iontronic pressure sensor with high sensitivity and linear response over a wide pressure range based on soft micropillared electrodes. *Sci. Bull.* **66**, 1091–1100 (2021).
- Chen, S. et al. Hierarchical elastomer tuned self-powered pressure sensor for wearable multifunctional cardiovascular electronics. *Nano Energy* **70**, 104460 (2020).
- Xu, J. et al. High sensitivity and broad linearity range pressure sensor based on hierarchical in-situ filling porous structure. *Npj Flex. Electron.* **6**, 62 (2022).
- Liu, Y., Pharr, M. & Salvatore, G. A. Lab-on-skin: A review of flexible and stretchable electronics for wearable health monitoring. *ACS Nano* **11**, 9614–9635 (2017).
- Sun, Q. J. et al. Fingertip-skin-inspired highly sensitive and multifunctional sensor with hierarchically structured conductive graphite/polydimethylsiloxane foams. *Adv. Funct. Mater.* **29**, 1808829 (2019).
- Kumar, S., Gupta, T. K. & Varadarajan, K. M. Strong, stretchable and ultrasensitive MWCNT/TPU nanocomposites for piezoresistive strain sensing. *Compos. Part B Eng.* **177**, 107285 (2019).
- Bae, K. et al. Dual-scale porous composite for tactile sensor with high sensitivity over an ultrawide sensing range. *Small* **18**, 2203193 (2022).
- Zhai, W. et al. Multifunctional flexible carbon black/polydimethylsiloxane piezoresistive sensor with ultrahigh linear range, excellent durability and oil/water separation capability. *Chem. Eng. J.* **372**, 373–382 (2019).
- Wu, X., Han, Y., Zhang, X., Zhou, Z. & Lu, C. Large-area compliant, low-cost, and versatile pressure-sensing platform based on microcrack-designed carbon black/polyurethane sponge for human-machine interfacing. *Adv. Funct. Mater.* **26**, 6246–6254 (2016).
- Zhang, H. et al. Pillared carbon@tungsten decorated reduced graphene oxide film for pressure sensors with ultra-wide operation range in motion monitoring. *Carbon* **189**, 430–442 (2022).

21. Zheng, Q., Lee, J., Shen, X., Chen, X. & Kim, J. Graphene-based wearable piezoresistive physical sensors. *Mater. Today* **36**, 158–179 (2020).
22. Zhu, G. et al. Highly-stretchable porous thermoplastic polyurethane/carbon nanotubes composites as a multimodal sensor. *Carbon* **195**, 364–371 (2022).
23. Chen, H. et al. Hybrid porous micro structured finger skin inspired self-powered electronic skin system for pressure sensing and sliding detection. *Nano Energy* **51**, 496–503 (2018).
24. Sencadas, V., Tawk, C. & Alici, G. Environmentally friendly and biodegradable ultrasensitive piezoresistive sensors for wearable electronics applications. *ACS Appl. Mater. Inter.* **12**, 8761–8772 (2020).
25. Song, Y. et al. All-in-one piezoresistive-sensing patch integrated with micro-supercapacitor. *Nano Energy* **53**, 189–197 (2018).
26. Nag, A. & Mukhopadhyay, S. C. Fabrication and implementation of carbon nanotubes for piezoresistive-sensing applications: A review. *J. Sci. Adv. Mater. Dev.* **7**, 100416 (2022).
27. Zhu, B. et al. Microstructured graphene arrays for highly sensitive flexible tactile sensors. *Small* **10**, 3625–3631 (2014).
28. Zhang, J. et al. Highly sensitive flexible three-axis tactile sensors based on the interface contact resistance of microstructured graphene. *Nanoscale* **10**, 7387–7395 (2018).
29. Chen, M. et al. Touchpoint-tailored ultrasensitive piezoresistive pressure sensors with a broad dynamic response range and low detection limit. *ACS Appl. Mater. Inter.* **11**, 2551–2558 (2019).
30. Tang, X. et al. Controllable graphene wrinkle for a high-performance flexible pressure sensor. *ACS Appl. Mater. Inter.* **13**, 20448–20458 (2021).
31. Shu, Y. et al. Surface-modified piezoresistive nanocomposite flexible pressure sensors with high sensitivity and wide linearity. *Nanoscale* **7**, 8636–8644 (2015).
32. Shi, J. et al. Multiscale hierarchical design of a flexible piezoresistive pressure sensor with high sensitivity and wide linearity range. *Small* **14**, 1800819 (2018).
33. Li, J., Wu, T., Jiang, H., Chen, Y. & Yang, Q. Ultrasensitive hierarchical piezoresistive pressure sensor for wide-range pressure detection. *Adv. Intell. Syst.* **3**, 2100070 (2021).
34. Jung, Y. et al. Irregular microdome structure-based sensitive pressure sensor using internal popping of microspheres. *Adv. Funct. Mater.* **32**, 2201147 (2022).
35. Zhao, T. et al. Pollen-shaped hierarchical structure for pressure sensors with high sensitivity in an ultrabroad linear response range. *ACS Appl. Mater. Inter.* **12**, 55362–55371 (2020).
36. Huang, Y. et al. Sensitive pressure sensors based on conductive micro-structured air-gap gates and two-dimensional semiconductor transistors. *Nat. Electron.* **3**, 59–69 (2020).
37. Bai, N. et al. Graded intrafilable architecture-based iontronic pressure sensor with ultra-broad-range high sensitivity. *Nat. Commun.* **11**, 209 (2020).
38. Boutry, C. M. et al. Biodegradable and flexible arterial-pulse sensor for the wireless monitoring of blood flow. *Nat. Biomed. Eng.* **3**, 47–57 (2019).
39. Mannsfeld, S. C. B. et al. Highly sensitive flexible pressure sensors with microstructured rubber dielectric layers. *Nat. Mater.* **9**, 859–864 (2010).
40. Li, W. et al. Flexible and high performance piezoresistive pressure sensors based on hierarchical flower-shaped SnSe₂nanoplates. *ACS Appl. Energy Mater.* **2**, 2803–2809 (2019).
41. Nie, P. et al. High-performance piezoresistive electronic skin with bionic hierarchical microstructure and microcracks. *ACS Appl. Mater. Inter.* **9**, 14911–14919 (2017).
42. Luo, Y. et al. Technology roadmap for flexible sensors. *ACS Nano* **17**, 5211–5295 (2023).
43. Nguyen, X. A., Gong, S., Cheng, W. & Chauhan, S. A stretchable gold nanowire sensor and its characterization using machine learning for motion tracking. *IEEE Sens. J.* **21**, 15269–15276 (2021).
44. Gao, Y. et al. Microchannel-confined MXene based flexible piezoresistive multifunctional micro-force sensor. *Adv. Funct. Mater.* **30**, 1909603 (2020).
45. Jian, M. et al. Flexible and highly sensitive pressure sensors based on bionic hierarchical structures. *Adv. Funct. Mater.* **27**, 1606066 (2017).
46. Han, S. et al. High-performance pressure sensors based on 3D microstructure fabricated by a facile transfer technology. *Adv. Mater. Technol.* **4**, 1800640 (2019).
47. Song, S. et al. Bioinspired engineering of gradient and hierarchical architecture into pressure sensors toward high sensitivity within ultra-broad working range. *Nano Energy* **100**, 107513 (2022).
48. Adepu, V., Kamath, K., Mattela, V. & Sahatiya, P. Development of Ti₃C₂Tx/NiSe₂nanohybrid-based large-area pressure sensors as a smart bed for unobtrusive sleep monitoring. *Adv. Mater. Inter.* **8**, 2100706 (2021).